Journal of Materials Chemistry A

PAPER

View Article Online
View Journal | View Issue

Published on 03 May 2018. Downloaded by University of Illinois Urbana-Champaign on 8/21/2022 11:49:56 PM.

Check for updates

Cite this: *J. Mater. Chem. A*, 2018, **6**, 10313

High efficiency electrochemical reduction of CO_2 beyond the two-electron transfer pathway on grain boundary rich ultra-small SnO_2 nanoparticles†

Chenglu Liang, ‡[ab] Byoungsu Kim, ‡[cd] Shize Yang, ‡[e] Yang Liu, [ab] Cristiano Francisco Woellner, [b] Zhengyuan Li, [b] Robert Vajtai, [b] Wei Yang, *[a] Jingjie Wu, *[f] Paul J. A. Kenis*[cd] and Pulickel M. Ajayan*[b]

Received 8th February 2018
Accepted 25th April 2018

DOI: 10.1039/c8ta01367e

rsc.li/materials-a

Well crystallized and interconnected SnO_2 nanoparticles (<5 nm) were synthesized *via* oxidation of exfoliated SnS_2 sheets. The SnO_2 nanoparticles exhibit a high total faradaic efficiency (FE) of 97% towards electrochemical reduction of CO_2 at −0.95 V *vs.* the reversible hydrogen electrode (RHE). The main product ratio of CO/$HCOO^-$ which intrinsically correlates to the surface SnO_x/Sn ratio variation varies with the applied potential. Beyond CO and $HCOO^-$ products formed *via* the two-electron transfer pathway, hydrocarbons and oxygenates are produced. The formation of hydrocarbon (CH_4) *versus* oxygenate (C_2H_5OH) depends on the choice of electrolyte (KOH *vs.* $KHCO_3$), both of which can reach a maximal faradaic efficiency of 10%. The distinctive grain boundary and exposed corner/step sites in the interconnected SnO_2 nanoparticles contribute to the high FE of CO_2 reduction and unique selectivity.

1. Introduction

Electrochemical reduction of CO_2 to fuels and chemical feedstock provides an attractive option to relieve the climate crisis and balance the carbon cycle to some extent. Developing efficient and stable catalysts for CO_2 reduction plays a decisive role in the conversion of chemically inert CO_2 to value-added chemicals. Metals,[1] metal complexes,[2–4] and alloys[5] have been exploited as electrocatalysts for CO_2 reduction in the past three decades. Cu based catalysts have attracted extensive attention because of their unparalleled ability of reducing CO_2 to multi-carbon products,[6,7] especially ethanol and ethylene.[8,9] Noble metals such as Au,[10] Ag[11,12] and Pd,[13] showed high selectivity for CO production. Among the non-precious metals, the low cost Sn-based catalysts exhibit high selectivity for formate,[14,15] a promising feedstock for fine chemicals.[16] Although the underlying mechanisms of Sn-based catalysts remain elusive concerning the reaction pathways and the nature of active sites, nanostructuring of tin and tin oxides has been experimentally demonstrated to be an effective way to improve the overall catalytic activities compared to their bulk counterparts. Xie *et al.*[15] developed metallic tin quantum sheets confined in graphene, which showed an enhanced faradaic efficiency of formate up to 89% with a current density of 21.1 mA cm^{-2} at −1.8 V *versus* SCE (saturated calomel electrode). Apart from using the Sn metal directly as catalysts, emerging evidence has proved that Sn oxide-derived Sn exhibited even better CO_2 reduction activity and tunable selectivity.[17–19] Kanan *et al.*[17] pointed out that SnO and SnO_2 formed rapidly on the surfaces of Sn when exposed to air.[20] The SnO_x layer persisted on electrode surfaces under the reduction conditions, which was essential for CO_2 reduction on the Sn-based catalyst as the etched electrode with fresh Sn^0 resulting in exclusive H_2 evolution. Modification of the nanostructure of the tin oxide precursors[18,21–24] has direct influences on the electrocatalytic performances of the reduced Sn catalysts. Further investigations on other oxide-derived metal catalysts including Au,[25] Cu[26] and Pb[27] by Kanan's group confirmed that the microstructure of metal oxides (*e.g.* high grain boundary density) determines CO_2 reduction activity/selectivity.

Herein, we developed a new method to synthesize well crystallized SnO_2 nanoparticles from exfoliated single or few layer SnS_2 sheets obtained *via* a cryo-exfoliation method.[28] The as-obtained SnO_2 nanoparticles combine the features of ultra-small size (<5 nm) and high crystallinity, which is difficult to

[a]College of Polymer Science and Engineering, Sichuan University, State Key Laboratory of Polymer Materials Engineering, Chengdu 610065, Sichuan, China
[b]Department of Materials Science and Nano Engineering, Rice University, 6100 Main Street, Houston, Texas 77005, USA
[c]Department of Chemical & Biomolecular Engineering, University of Illinois at Urbana-Champaign, 600 South Mathews Avenue, Urbana, IL 61801, USA
[d]International Institute for Carbon Neutral Energy Research (WPI-I2CNER), Kyushu University, 744 Moto-oka, Nishi-ku, Fukuoka, 819-0395, Japan
[e]Materials Science and Technology Division, Oak Ridge National Laboratory, Oak Ridge, Tennessee 37831, USA
[f]Department of Chemical and Environmental Engineering, University of Cincinnati, Cincinnati, OH 45221, USA. E-mail: jingjie.wu@uc.edu

† Electronic supplementary information (ESI) available. See DOI: 10.1039/c8ta01367e

‡ The authors contributed equally to this work.

Published on 03 May 2018. Downloaded by University of Illinois Urbana-Champaign on 8/21/2022 11:49:56 PM.

achieve by traditional wet chemical methods including sol–gel,[29] hydrothermal processes,[30] microwave heating methods,[31] and sonochemical synthesis.[32] These prior methods produce SnO_2 nanoparticles with a low crystallinity, thus further annealing at higher temperatures was necessary to achieve satisfactory crystallinity, which in turn resulted in crystal growth to form bigger nanoparticles.[29,31] In addition, our ultra-small SnO_2 nanoparticles are interconnected to each other to form a distinguished grain boundary. The ultra-small SnO_2 nanoparticles showed a high faradaic efficiency (FE) of ~97% for CO_2 reduction at −0.95 eV *vs.* RHE. Most intriguingly, hydrocarbons and oxygenates were first formed beyond CO and $HCOO^-$ on Sn-based catalysts, of which methane (CH_4) or ethanol (C_2H_5OH) is the main product with a yield up to a FE of 10% depending on the electrolyte. The reaction mechanism of our catalyst, ultrasmall SnO_2 nanoparticles, is different from that of the traditional Sn catalyst. Our work suggests that electrocatalytic activity and selectivity of Sn based catalysts toward CO_2 reduction can be tuned by nanostructuring.

2. Materials and methods

2.1 Synthesis of bulk SnS_2

2 mmol $SnCl_4 \cdot 5H_2O$ and 15 mmol thioacetamide (CH_3CSNH_2) were added to 80 mL distilled water. After vigorous stirring for 10 min to dissolve both $SnCl_4 \cdot 5H_2O$ and thioacetamide, the mixture was transferred into a 100 mL Teflon-lined autoclave, sealed and heated at 180 °C for 24 h to form bulk SnS_2. After cooling down to room temperature naturally, the hydrothermally treated mixture was centrifuged to get the sediment of the bulk SnS_2 product. The bulk SnS_2 was washed with distilled water and absolute ethanol many times until the supernate of the bulk SnS_2 suspension became colorless with a pH value of about 7. The as-obtained bulk SnS_2 was dried at 50 °C for 48 h and then the bulk SnS_2 powder was annealed at 400 °C for 1 h under the flow of argon protection to remove sulfur residual in SnS_2. And the bulk SnO_2 was obtained by annealing bulk SnS_2 at 500 °C for 3 h under air conditions.

2.2 Exfoliation of SnS_2

The bulk SnS_2 was firstly cryogenically treated followed by sonication in H_2O for 4 h. After sonication, the as-obtained suspension was centrifuged at 10 000 rpm for 30 min to get the supernate which contained mainly single or few layer SnS_2 sheets.

2.3 SnO_2 nanoparticles derived from SnS_2 sheets

40 mL of the supernate of SnS_2 sheets (~0.2 mg mL^{-1}) was mixed with 5 mL of 30 wt% H_2O_2 aqueous solution under stirring. Then the mixture was transferred into a Teflon-lined stainless steel autoclave, sealed and heated at 200 °C for 24 h. After the hydrothermal process, the SnS_2 sheets were transformed into well crystallized SnO_2 nanoparticles.

2.4 Electrochemical measurements

The CO_2 reduction reaction was conducted in an electrochemical flow cell employing SnO_2 nanoparticle-based gas diffusion electrodes. The schematic of the flow cell for CO_2 reduction is presented in the ESI (Fig. S1).† The electrolysis was performed in a potentiostatic mode with a full cell voltage ranging from −1.65 to −3.5 V controlled using a potentiostat (Autolab PGSTAT-30, EcoChemie) under ambient pressure and temperature. While both the catholyte and anolyte were 1 M KOH, the pH value of 1 M KOH was calibrated to be 13.48 by using a pH meter (Thermo Orion, 9106BNWP). CO_2 was supplied to the cathode side. A syringe pump (PHD 2000, Harvard Apparatus) supplied the electrolyte (1 M KOH) to minimize boundary layer depletion effects and supply fresh electrolytes thereby helping to maintain the pH on the electrode surface. Individual electrode potentials were recorded using multimeters (AMPROBE 15XP-B) connected to each electrode and a reference electrode (Ag/AgCl; RE-5B, BASi) placed in the electrolyte exit stream. The measured potentials after *iR* compensation were rescaled to the RHE using the equation E (*versus* RHE) = E (*versus* Ag/AgCl) + 0.209 V + 0.0591 V × pH. The current reported here was obtained by averaging the span of time (at least 180 s) for each applied voltage.

For each applied voltage, after the cell reached the steady state, 1 mL of the effluent gas stream was periodically sampled and diverted into a gas chromatograph (Thermo Finnegan Trace GC) equipped with both thermal conductivity and flame ionization detectors, and a Carboxen 1000 column (Supelco). Also, the exit catholyte was collected at each applied voltage followed by identifying and quantifying using ^1H NMR (nuclear magnetic resonance, UI500NB, Varian). In addition to gaseous products from the electrochemical CO_2 reduction reaction, H_2 was detected as the product of the competing hydrogen evolution reaction.

The working electrode was prepared by mixing 20 mL of the catalyst suspension with 50 μL of Nafion solution (0.5 wt%) followed by sonication for 15 min. The catalyst ink was then spray coated onto a gas diffusion layer (GDL, Sigracet 35 BC) with an area of 0.5 mm × 2.0 mm, which was then dried for 24 h before the CO_2 reduction experiments. The counter electrodes, anodes, were prepared by hand-painting of IrO_2 catalyst ink onto the GDL to reach a loading of about 1.5 mg cm^{-2}.

3. Results and discussion

The synthetic process of SnO_2 nanoparticles is displayed in Scheme 1. SnS_2 nanosheets were prepared by liquid phase exfoliation of the bulk SnS_2 powder in H_2O. The thickness of SnS_2 nanosheets is in the range of 0.8–1.8 nm as shown in the AFM profile (Fig. S2, ESI†), indicating the existence of single or few layer SnS_2 sheets. The TEM images of SnS_2 sheets show the

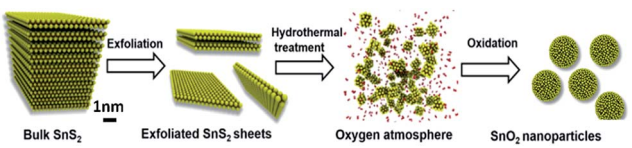

Scheme 1 Schematic illustration of the synthesis of uniform SnO_2 nanoparticles.

 This journal is © The Royal Society of Chemistry 2018

Published on 03 May 2018. Downloaded by University of Illinois Urbana-Champaign on 8/21/2022 11:49:56 PM.

nanosheet morphology (Fig. S2, ESI†). The XRD (Fig. 1a) and Raman spectroscopy (Fig. 1b) results further confirm the successful exfoliation of bulk SnS_2 into SnS_2 nanosheets. The bulk SnS_2 shows typical diffraction peaks at 15.0 (001), 28.2 (100), 30.2 (002), 32.1 (101), 46.1 (003), 49.9 (110), 52.4 (111), 62.9 (004), 67.1 (202) and 70.3° (113) for 1T-SnS_2 (JCPDS no. 23-0677). After exfoliation, the XRD diffraction pattern only shows *c*-axis orientation peaks for ⟨001⟩ faces indicating the successful exfoliation of bulk SnS_2 into SnS_2 nanosheets. The Raman spectra of both bulk SnS_2 and SnS_2 nanosheets display a peak centered at 314 cm^{-1} attributed to the A_{1g} vibration mode of SnS_2.[33] Then the exfoliated SnS_2 sheets were used as precursors to synthesize SnO_2 nanoparticles by hydrothermal heating at 200 °C for 24 h in the presence of excess H_2O_2 aqueous solution (oxidizing agent). The corresponding XRD pattern displays diffraction peaks of only SnO_2 (JCPDS no. 77-0450) at 26.5 (110), 33.9 (101), 37.9 (200), 51.9 (211), 54.9 (220), 57.9 (002), 61.8 (310), 64.6 (112), 66.2 (301), 71.4 (202) and 79.0 (321), which is consistent with the XRD results of the bulk SnO_2 obtained by annealing bulk SnS_2 at 500 °C for 3 h under air conditions, indicating the formation of SnO_2. The bulk SnO_2 shows a main Raman peak at about 635 cm^{-1} for the A_{1g} vibration mode of typical SnO_2 along with two minor peaks at about 475 cm^{-1} and 775 cm^{-1} for the E_g and B_{2g} modes, respectively.[34] As a comparison, the A_{1g} vibration mode of SnO_2 nanoparticles red shifts to 618 cm^{-1} and the peaks are broadened, both indicating the nature of nanocrystalline materials.[35] XPS spectra shown in Fig. 1c and d further confirm the transformation of SnS_2 nanosheets into SnO_2 nanoparticles. The Sn_{3d} spectra of SnS_2 nanosheets show mainly the Sn(IV) feature of SnS_2 at $3d_{3/2}$ 495.3 eV and $3d_{5/2}$ 486.9 eV. There are two shoulder peaks at 494.0 eV and 485.6 eV corresponding to Sn(II) species,[36,37] which is most probably due to the tendency of SnS_2 to lose sulfur atoms. After the SnS_2 nanosheets were oxidized to SnO_2, the Sn_{3d} spectra show only the Sn(IV) feature of SnO_2 at 495.8 eV and 487.4 eV for $3d_{3/2}$ and $3d_{5/2}$ binding energies, respectively.[38] The O 1s spectrum of SnO_2 nanoparticles in Fig. 1d can be deconvoluted into peaks at 530.2 eV for the lattice oxygen (Sn–O–Sn) in SnO_2, at 531.2 eV for Sn–O, and at 532.4 eV for the absorbed surface oxygen.[39,40] Besides, the S 2p XPS spectra shown in Fig. S3† can provide further evidence for the complete transformation from SnS_2 to SnO_2. The S 2p XPS spectrum of original SnS_2 nanosheets can be deconvoluted into two peaks at 162.9 eV and 161.7 eV, corresponding to the $2p_{1/2}$ and $2p_{3/2}$ binding energies of SnS_2.[37,41] When oxidized to SnO_2 nanoparticles, the sulfide was transformed to sulfate which shows higher binding energies at 169.8 eV and 168.6 eV for the $2p_{1/2}$ and $2p_{3/2}$, respectively.[42,43]

Interestingly, the morphology of layered SnS_2 nanosheets was transformed into uniform nanoparticles of SnO_2 after the hydrothermal reaction. TEM images of SnO_2 nanoparticles are presented in Fig. 2a–c with different magnifications. Low magnification view shows the aggregation of small nanoparticles. A single nanoparticle (diameter about 5 nm or smaller) with well-defined crystal facets can be distinguished at high magnifications. The SnO_2 nanoparticles (or grains) interconnect with each other to form a grain boundary (Fig. 2b, c and S3†). The measured interplanar spacing is 0.335 nm, 0.264 nm and 0.176 nm corresponding to the (110), (101) and (211) of SnO_2, respectively, which are consistent with the XRD results. Electron energy-loss spectroscopy (EELS) of the sample (Fig. 2d) displays two sharp peaks at 532 eV and 538 eV along with a broad peak at about 555 eV, which agrees with the identity of SnO_2.[44] AFM and more TEM pictures of SnO_2 nanoparticles are shown in Fig. S4,† displaying a typical morphology of nanoparticles. The SnO_2 particles converted from bulk SnS_2 showed a morphology of aggregated particles with the size ranging from

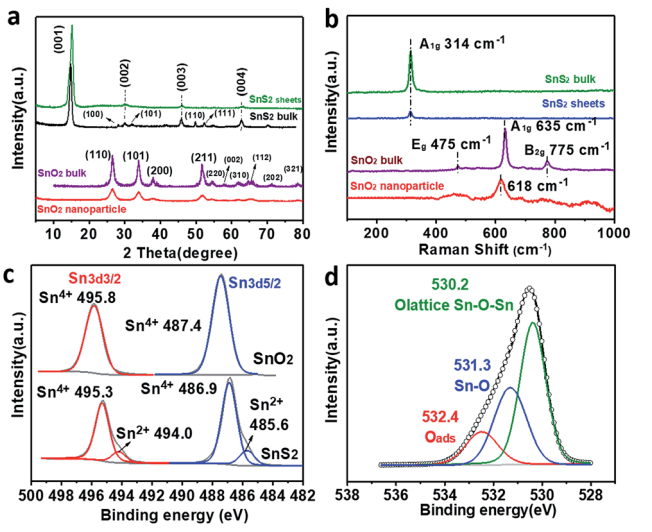

Fig. 1 (a) XRD patterns and (b) Raman spectra of exfoliated SnS_2 nanosheets, bulk SnS_2, SnO_2 nanoparticles and bulk SnO_2, (c) Sn 3d XPS spectra of SnS_2 nanosheets and SnO_2 nanoparticles, (d) O 1s XPS spectrum of SnO_2 nanoparticles.

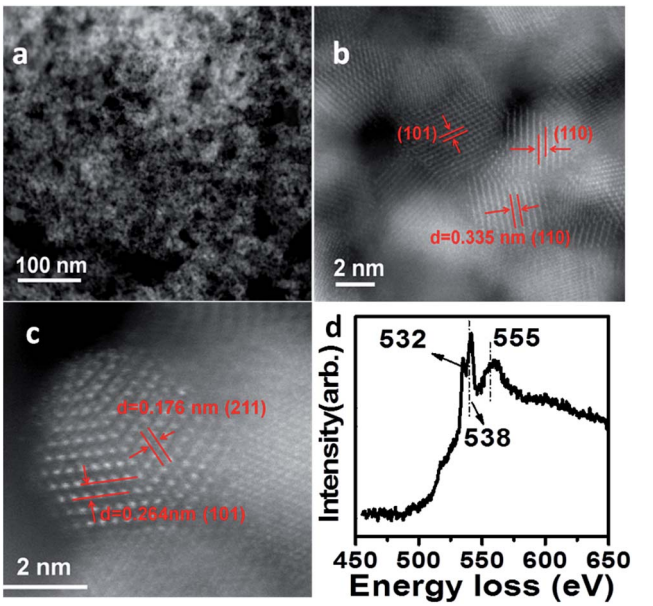

Fig. 2 TEM image of SnO_2 nanoparticles with (a) a low magnification, (b) and (c) with a high magnification, and (d) electron energy-loss spectroscopy (EELS) of SnO_2 NPs.

Published on 03 May 2018. Downloaded by University of Illinois Urbana-Champaign on 8/21/2022 11:49:56 PM.

200 nm to 500 nm as shown in the SEM image (Fig. S5†). The crystallite size of bulk SnO_2 particles was calculated to be around 28 nm using the Debye–Scherrer equation from the XRD results.

The electrocatalytic activity of SnO_2 nanoparticles towards CO_2 reduction was evaluated in 1 M KOH electrolyte in a flow cell which incorporates a gas diffusion electrode coated with a SnO_2 nanoparticle catalyst. The applied cathodic potentials ranged from −0.20 to −1.10 V *versus* the reversible hydrogen electrode (RHE). The overall faradaic efficiency (FE) of CO_2 reduction increased as the potential was swept more negatively, from 10% at −0.26 V to a maximum of 97% at −0.95 V as shown in Fig. 3a. Interestingly, when the applied potential was more positive than −0.62 V, CO was the only reduction product, which is uncommon in Sn catalysts usually preferring $HCOO^-$ selectivity. When the applied potential was negatively beyond −0.62 V, $HCOO^-$ became the predominant product. The maximum FE of $HCOO^-$ achieved a value of 74% at −0.73 V. One exclusive property for SnO_2 nanoparticles is that the total FE of CO_2 reduction reaches a maximum of 97% at −0.95 V. Another unique selectivity for SnO_2 nanoparticles is that trace amounts of hydrocarbons (CH_4 and C_2H_4 < 1% FE) emerged at −0.73 and −0.8 V, respectively. On further increasing the potentials to −0.95 V and −1.03 V, noticeable amounts of 7% CH_4 and 14% CH_4 were detected, respectively, along with trace amounts of C_2H_4, C_2H_5OH, CH_3COOH and *n*-C_3H_7OH, which was never reported for the Sn-catalyst for electrochemical CO_2 reduction.

For the SnS_2 nanosheet electrode (Fig. 3b), the H_2 evolution reaction dominates over CO_2 reduction. Among CO_2 reduction products, $HCOO^-$ was the main product in the applied potential range of −0.26 to −0.80 V, but only reached a maximum FE of about 37% at −0.62 V. The dominant selectivity of $HCOO^-$ over SnS_2 nanosheets is consistent with typical Sn based catalysts. For the bulk SnO_2 particle electrode, CO appeared as the primary product with a FE of about 32% at −0.45 V and then

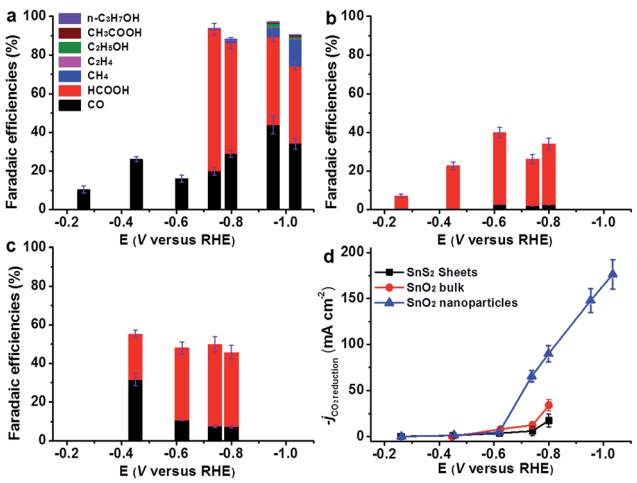

Fig. 3 Faradaic efficiencies for CO_2 reduction at various applied potentials for (a) SnO_2 nanoparticles, (b) SnS_2 nanosheets and (c) bulk SnO_2 particles. (d) The CO_2 current densities for three electrodes evaluated in 1 M KOH electrolyte.

$HCOO^-$ became the major product at more negative potentials, reaching a maximum FE of 42% at −0.74 V (Fig. 3c). Neither SnS_2 nanosheets nor bulk SnO_2 particles yielded hydrocarbon and oxygenate products. In addition, the maximum total FE of CO_2 reduction over either SnS_2 nanosheets (~40%) or bulk SnO_2 particles (~55%) is much lower than that for SnO_2 nanoparticles (~97%). The unique selectivity to hydrocarbons/oxygenates and high FE of SnO_2 nanoparticles different from the bulk counterparts is derived from their distinctive structure: the active grain boundary and exposed corner sites and edge sites in the reduced size (<5 nm). High density of grain boundaries in SnO_2 nanoparticles is responsible for the active surfaces for enhanced CO_2 reduction[45,46] and the adsorption/desorption of key intermediates like $^{\bullet}CO_2^-$ and CO at the grain boundaries may be tailored towards the formation of more reduced products like hydrocarbons/oxygenates.[47] Likewise, the stabilization of the $^{\bullet}CO_2^-$ intermediate in the ultra-small SnO_2 nanoparticles over the bulk SnO_2 or the SnS_2 with a larger size[15,18] facilitated CO_2 reduction over the competing HER and contributed to the high FE (~97%) of CO_2 reduction.

The current densities of CO_2 reduction for three electrodes are summarized in Fig. 3d. The current density of SnO_2 nanoparticle electrode increased drastically with the applied potentials beyond −0.62 V, and achieved beyond 100 mA cm^{-2} after −0.8 V. In contrast, the current density of CO_2 reduction is only 34 mA cm^{-2} at −0.8 V for SnO_2 bulk particles and 17 mA cm^{-2} at −0.8 V for SnS_2 nanosheets. The enhanced current density of CO_2 reduction for SnO_2 nanoparticles is largely due to their higher intrinsic activity towards CO_2 reduction.

The linear sweep voltammetry (LSV) measurements were firstly carried out in Ar_2-saturated 1 M KOH and the results are shown in Fig. S6.† As revealed by LSV, the SnO_2 nanoparticles exhibited the highest current density among the samples, which was roughly 2 and 3 times larger than those of SnS_2 sheets and SnO_2 bulk, respectively, indicating the high catalytic potential in SnO_2 nanoparticles. The comparison of LSV in Ar_2 and CO_2 saturated 0.1 M $KHCO_3$ shows the typical increasing of current density in the CO_2 saturated electrolyte, a potential indicator of CO_2 reduction activity on SnO_2 nanoparticles.

Also, the noticeable amounts of 5% CH_4 and 14% CH_4 detected at applied potentials of −0.95 V and −1.03 V respectively, should be emphasized (Fig. S7†). It is interesting to find that when the SnO_2 nanoparticle catalyst was tested in $KHCO_3$ electrolyte, the selectivity for C_2H_5OH is higher over CH_4, reaching a FE of ~6% at −1.05 V apart from the main products of CO (FE of 35%) and $HCOO^-$ (FE of 19%) as shown in Fig. S8.† While the applied potential was more negative (−1.21 V), a higher FE of $HCOO^-$ (~40%) was achieved. After the electrolysis of the SnO_2 nanoparticle catalyst for 30 min, the FE of C_2H_5OH increased from 6% to 10% at −1.05 V and from 3% to 6% at −1.21 V, possibly due to the surface component change in the metastable SnO_x layer after electrolysis under reduction potentials for 30 min. The potential of getting minor CO_2 reduction products was reported in typical transition metal catalysts with known high selectivity towards CO or $HCOO^-$ (ref. 48 and 49) by Jaramillo's group. They observed formate, methane, methanol, and ethanol as minor products for an Ag

 This journal is © The Royal Society of Chemistry 2018

Published on 03 May 2018. Downloaded by University of Illinois Urbana-Champaign on 8/21/2022 11:49:56 PM.

Table 1 Comparison of CO_2 reduction performance for Sn-based electrocatalysts[a]

Catalysts	Electrolytes	Potential at FE_{max} (V *vs.* RHE)	FE_{max} (%)		$-j_{CO_2\ reduction}$ (mA cm^{-2})	Ref.
			CO	$HCOO^-$		
100 nm Sn particles	0.5 M $KHCO_3$	−0.9	Not reported	80	~12	55
Electrodeposited Sn particles (~500 nm)	0.1 M $KHCO_3$	−1.19	Not reported	83.5	~7.6	56
Electrodeposited Sn (~1 μm thick)	0.5 M $NaHCO_3$	−1.05	10	71	~10	14
In situ deposited Sn/SnO_x thin film (a porous, particulate film)	0.5 M $NaHCO_3$	−0.7	~56	~40	3–4	17
Tin quantum sheets (~5 nm)	0.1 M $NaHCO_3$	−1.15	Not reported	>85	21.1	15
Nano-SnO_2 (3–200 nm particles)	0.1 M $NaHCO_3$	−1.15	Not reported	93.6	~9.8	18
Cu/SnO_2 core/shell structure with 0.8 nm SnO_2 shell	0.5 M $KHCO_3$	−0.7	93	0	4.6	19
Cu/SnO_2 core/shell structure with 1.8 nm SnO_2 shell		−0.9	<1	85	Not reported	
Ultra-small SnO_2 nanoparticles (<5 nm)	1 M $KHCO_3$	−1.21	16	64	145	This work
	1 M KOH	−0.95	44	46	147	

[a] Note: all the applied potentials were converted to the RHE scale. $E(RHE) = E(Ag/AgCl) + 0.0591\ V \times pH + 0.209\ V$, $E(RHE) = E(SCE) + 0.0591\ V \times pH + 0.242\ V$ (01 M $KHCO_3$/$NaHCO_3$ pH = 6.8, 0.5 M $KHCO_3$/$NaHCO_3$ pH = 7.6, 1 M $KHCO_3$ pH = 9.2).

catalyst,[50] which usually produce CO as the main product. In our work, it was found that the selectivity of the minor product was influenced by the electrolyte. When KOH was used as the electrolyte, the minor product was mainly CH_4. In $KHCO_3$ electrolyte, C_2H_5OH emerged as the primary minor product. The influence of electrolytes can be ascribed to their different modulations of the local pH value on the electrode surface, which in turn influences the availability of protons on the surface. The availability of protons and the H(ads) coverage on the electrode will have a strong influence on the protons involved in the CO_2 reduction reaction and HER. In our system, the delicate catalyst–electrolyte interplay may influence not only the H(ads) coverage, but also the C–C coupling between C1 species at an early stage. In KOH electrolyte, the HER was suppressed due to the strong alkaline condition and the consumption of OH^- by reacting with $CO_2(g)$ to form HCO_3^- can lower the local pH value. However in $KHCO_3$ electrolyte, the FE of the HER increased, which increased the local pH value by producing more OH^-. Besides, the negatively charged key intermediates, such as the adsorbed $^{\cdot}CO^{2-}$ anion and the adsorbed $(CO)^{2-}$ anionic dimer are particularly sensitive to pH and solvent effects, which may alter the reaction probability between the C1 and C2 pathways.[51]

Apart from the minor products, CO or $HCOO^-$ was still the main reduction product in our system. Comparison of FEs and current densities of CO or $HCOO^-$ reported for Sn-based catalysts is shown in Table 1. The analysis of the results in Table 1 indicates that the selectivity of CO and $HCOO^-$ could be tailored by modifying the surface chemistry and structure of the Sn catalyst. When the metal Sn (with a native SnO_x layer) was used directly as the catalyst, the main product is $HCOO^-$. However, when tin oxide is utilized as the catalyst, the CO product can be predominant depending on the oxide thickness. An ultra-thin layer of extrinsic SnO_x favors the production of CO over $HCOO^-$, which was demonstrated in the cases of an *in situ*-deposited Sn/SnO_x thin film[17] (thickness of Sn/SnO_x thin film was not mentioned in the work) and a Cu/SnO_2 core/shell structure with a 0.8 nm SnO_2 shell,[19] reaching a high CO FE of ~56 and 93, respectively. For our SnO_2 nanoparticles, CO was the only reduction product of CO_2 at low overpotentials (−0.26 to −0.62 V *vs.* RHE). With the potentials swept more negatively beyond −0.62 V, the $HCOO^-$ emerged as the main product. The switch of selectivity between CO and $HCOO^-$ may be related to the chemical state of the Sn surface. At low overpotentials, the applied negative potentials may not be able to achieve a high degree of SnO_2 reduction. Thus an ultra-thin metastable SnO_x/Sn layer was formed initially, which may lead to the high selectivity of CO. When the potentials were swept more negatively beyond −0.62 V, more SnO_2 was prone to be reduced to metal Sn, especially in the ultra-small SnO_2 nanoparticles, and the content of Sn in the metastable SnO_x/Sn increased. As a result, the high selectivity of $HCOO^-$ showed up like for other typical Sn based catalysts. It is worth mentioning that even if the applied potentials were much more negative than the standard reduction potential of SnO_2 (~−0.35 V *vs.* RHE), a layer of metastable SnO_x still persists[17,18,52–54] due to kinetic limitations.

4. Conclusion

Taking advantage of the ultra-thin exfoliated SnS_2 nanosheet framework, ultra-small, interconnected, and well crystallized SnO_2 nanoparticles (<5 nm) were synthesized *via* simple oxidation. When used as an electrocatalyst for reduction of CO_2, SnO_2 nanoparticles exhibited a high total faradaic efficiency of 97% at −0.95 V *vs.* the reversible hydrogen electrode (RHE) accompanied by a high current density of 147 mA cm^{-2}. In addition, except the typical CO_2 reduction products of CO and $HCOO^-$ for Sn-based catalysts, CH_4 and C_2H_5OH were detected in KOH and $KHCO_3$ electrolytes, with a faradaic efficiency up to 10%. The unique structure of interconnected SnO_2 nanoparticles lead to a promising total FE of 97% at relatively low overpotentials and distinctive selectivity that was never reported for other Sn-based catalysts. The grain boundary between the crystallized SnO_2 nanoparticles may serve as active sites for the formation of hydrocarbons and oxygenates. The surface SnO_x/Sn ratio may play a key role in determining the formation of CO *versus* $HCOO^-$, which in turn influences the route to form hydrocarbons and oxygenates.

Published on 03 May 2018. Downloaded by University of Illinois Urbana-Champaign on 8/21/2022 11:49:56 PM.

Conflicts of interest

There are no conflicts to declare.

Acknowledgements

This research is financially supported by SABIC. Chenglu Liang also would like to thank the financial support from the China Scholarship Council during her study in Rice University. The electron microscopy (S. Z. Y.) was supported in part by the U.S. Department of Energy, Office of Science, Basic Energy Sciences, Materials Science and Engineering Division and through a user proposal supported by ORNL's Center for Nanophase Materials Sciences, which is sponsored by the Scientific User Facilities Division of the U.S. Department of Energy.

Notes and references

1 J. Medina-Ramos, R. C. Pupillo, T. P. Keane, J. L. DiMeglio and J. Rosenthal, *J. Am. Chem. Soc.*, 2015, **137**, 5021–5027.
2 L. Chen, Z. Guo, X.-G. Wei, C. Gallenkamp, J. Bonin, E. Anxolabéhère-Mallart, K.-C. Lau, T.-C. Lau and M. Robert, *J. Am. Chem. Soc.*, 2015, **137**, 10918–10921.
3 C. Costentin, M. Robert and J.-M. Savéant, *Acc. Chem. Res.*, 2015, **48**, 2996–3006.
4 J. Shen, R. Kortlever, R. Kas, Y. Y. Birdja, O. Diaz-Morales, Y. Kwon, I. Ledezma-Yanez, K. P. Schouten, G. Mul and M. T. M. Koper, *Nat. Commun.*, 2015, **6**, 8177.
5 M. Watanabe, M. Shibata, A. Kato, M. Azuma and T. Sakata, *J. Electrochem. Soc.*, 1991, **138**, 3382–3389.
6 M. Ma, K. Djanashvili and W. A. Smith, *Angew. Chem.*, 2016, **128**, 6792–6796.
7 D. Ren, N. Wong, A. Handoko, Y. Huang and B. Yeo, *J. Phys. Chem. Lett.*, 2016, **7**, 20–24.
8 S. F. Roberts, K. P. Kuhl and A. Nilsson, *Angew. Chem., Int. Ed.*, 2015, **54**, 5179–5182.
9 H. Mistry, A. Varela, C. S. Bonifacio, I. Zegkinoglou, I. Sinev, Y.-W. Choi, K. Kisslinger, E. A. Stach, J. C. Yang, P. Strasser and B. Cuenya, *Nat. Commun.*, 2016, **7**, 12123.
10 H.-E. Lee, K. Yang, S. Yoon, H.-Y. Ahn, Y. Lee, H. Chang, D. Jeong, Y.-S. Lee, M. Kim and K. Nam, *ACS Nano*, 2015, **9**, 8384–8393.
11 C. Kim, H. Jeon, T. Eom, M. Jee, H. Kim, C. M. Friend, B. Min and Y. Hwang, *J. Am. Chem. Soc.*, 2015, **137**, 13844–13850.
12 J. Rosen, G. S. Hutchings, Q. Lu, S. Rivera, Y. Zhou, D. G. Vlachos and F. Jiao, *ACS Catal.*, 2015, **5**, 4293–4299.
13 D. Gao, H. Zhou, J. Wang, S. Miao, F. Yang, G. Wang, J. Wang and X. Bao, *J. Am. Chem. Soc.*, 2015, **137**, 4288–4291.
14 E. Irtem, T. Andreu, A. Parra, M. D. Hernandez-Alonso, S. Garcia-Rodriguez, J. M. Riesco-Garcia, G. Penelas-Perez and J. R. Morante, *J. Mater. Chem. A*, 2016, **4**, 13582–13588.
15 F. Lei, W. Liu, Y. Sun, J. Xu, K. Liu, L. Liang, T. Yao, B. Pan, S. Wei and Y. Xie, *Nat. Commun.*, 2016, **7**, 12697.
16 M. G. Mura, L. D. Luca, G. Giacomelli and A. Porcheddu, *Adv. Synth. Catal.*, 2012, **354**, 3180–3186.
17 Y. Chen and M. W. Kanan, *J. Am. Chem. Soc.*, 2012, **134**, 1986–1989.
18 S. Zhang, P. Kang and T. J. Meyer, *J. Am. Chem. Soc.*, 2014, **136**, 1734–1737.
19 Q. Li, J. Fu, W. Zhu, Z. Chen, B. Shen, L. Wu, Z. Xi, T. Wang, G. Lu, J.-j. Zhu and S. Sun, *J. Am. Chem. Soc.*, 2017, **139**, 4290–4293.
20 G. B. Hoflund and G. R. Corallo, *Phys. Rev. B: Condens. Matter Mater. Phys.*, 1992, **46**, 7110–7120.
21 F. Li, L. Chen, G. P. Knowles, D. R. MacFarlane and J. Zhang, *Angew. Chem., Int. Ed.*, 2017, **56**, 505–509.
22 Y. Liu, M. Fan, X. Zhang, Q. Zhang, D. Guay and J. Qiao, *Electrochim. Acta*, 2017, **248**, 123–132.
23 J. Wu, F. G. Risalvato, S. Ma and X.-D. Zhou, *J. Mater. Chem. A*, 2014, **2**, 1647–1651.
24 B. Kumar, V. Atla, P. J. Brian, S. Kumari, T. Nguyen, M. Sunkara and J. M. Spurgeon, *Angew. Chem., Int. Ed.*, 2017, **56**, 3645–3649.
25 Y. Chen, C. W. Li and M. W. Kanan, *J. Am. Chem. Soc.*, 2012, **134**, 19969–19972.
26 C. W. Li and M. W. Kanan, *J. Am. Chem. Soc.*, 2012, **134**, 7231–7234.
27 C. H. Lee and M. W. Kanan, *ACS Catal.*, 2015, **5**, 465–469.
28 Y. Wang, Y. Liu, J. Zhang, J. Wu, H. Xu, X. Wen, X. Zhang, C. S. Tiwary, W. Yang, R. Vajtai, Y. Zhang, N. Chopra, I. N. Odeh, Y. Wu and P. M. Ajayan, *Sci. Adv.*, 2017, **3**, e1701500.
29 C. H. Shek, J. K. L. Lai and G. M. Lin, *Nanostruct. Mater.*, 1999, **11**, 887–893.
30 S. Fujihara, T. Maeda, H. Ohgi, E. Hosono, H. Imai and S.-H. Kim, *Langmuir*, 2004, **20**, 6476–6481.
31 J.-J. Zhu, J.-M. Zhu, X.-H. Liao, J.-L. Fang, M.-G. Zhou and H.-Y. Chen, *Mater. Lett.*, 2002, **53**, 12–19.
32 J. Zhu, Z. Lu, S. T. Aruna, D. Aurbach and A. Gedanken, *Chem. Mater.*, 2000, **12**, 2557–2566.
33 C. Wang, K. Tang, Q. Yang and Y. Qian, *Chem. Phys. Lett.*, 2002, **357**, 371–375.
34 R. S. Katiyar, P. Dawson, M. M. Hargreave and G. R. Wilkinson, *J. Phys. C: Solid State Phys.*, 1971, **4**, 2421.
35 A. Diéguez, A. Romano-Rodríguez, A. Vilà and J. R. Morante, *J. Appl. Phys.*, 2001, **90**, 1550–1557.
36 S. Axnanda, Z. Zhu, W. Zhou, B. Mao, R. Chang, S. Rani, E. Crumlin, G. Somorjai and Z. Liu, *J. Phys. Chem. C*, 2014, **118**, 1935–1943.
37 T. J. Whittles, L. A. Burton, J. M. Skelton, A. Walsh, T. D. Veal and V. R. Dhanak, *Chem. Mater.*, 2016, **28**, 3718–3726.
38 J.-M. Themlin, M. Chtaïb, L. Henrard, P. Lambin, J. Darville and J.-M. Gilles, *Phys. Rev. B: Condens. Matter Mater. Phys.*, 1992, **46**, 2460–2466.
39 A. R. Babar, S. S. Shinde, A. V. Moholkar, C. H. Bhosale, J. H. Kim and K. Y. Rajpure, *J. Semicond.*, 2011, **32**, 053001.
40 M. Kwoka, L. Ottaviano, M. Passacantando, S. Santucci, G. Czempik and J. Szuber, *Thin Solid Films*, 2005, **490**, 36–42.
41 K. Laajalehto, I. Kartio and P. Nowak, *Appl. Surf. Sci.*, 1994, **81**, 11–15.
42 A. A. Audi and P. M. A. Sherwood, *Surf. Interface Anal.*, 2000, **29**, 265–275.
43 M. Wahlqvist and A. Shchukarev, *J. Electron Spectrosc. Relat. Phenom.*, 2007, **156**, 310–314.

 This journal is © The Royal Society of Chemistry 2018

Published on 03 May 2018. Downloaded by University of Illinois Urbana-Champaign on 8/21/2022 11:49:56 PM.

44 M. S. Moreno, R. F. Egerton and P. A. Midgley, *Phys. Rev. B: Condens. Matter Mater. Phys.*, 2004, **69**, 233304.
45 X. Feng, K. Jiang, S. Fan and M. W. Kanan, *J. Am. Chem. Soc.*, 2015, **137**, 4606–4609.
46 C. W. Li, J. Ciston and M. W. Kanan, *Nature*, 2014, **508**, 504.
47 R. G. Mariano, K. McKelvey, H. S. White and M. W. Kanan, *Science*, 2017, **358**, 1187.
48 K. P. Kuhl, T. Hatsukade, E. R. Cave, D. N. Abram, J. Kibsgaard and T. F. Jaramillo, *J. Am. Chem. Soc.*, 2014, **136**, 14107–14113.
49 E. R. Cave, J. H. Montoya, K. P. Kuhl, D. N. Abram, T. Hatsukade, C. Shi, C. Hahn, J. K. Norskov and T. F. Jaramillo, *Phys. Chem. Chem. Phys.*, 2017, **19**, 15856–15863.
50 T. Hatsukade, K. P. Kuhl, E. R. Cave, D. N. Abram and T. F. Jaramillo, *Phys. Chem. Chem. Phys.*, 2014, **16**, 13814–13819.
51 R. Kortlever, J. Shen, K. P. Schouten, F. Calle-Vallejo and M. T. M. Koper, *J. Phys. Chem. Lett.*, 2015, **6**, 4073–4082.
52 Y. Zhang, L. Chen, F. Li, C. D. Easton, J. Li, A. M. Bond and J. Zhang, *ACS Catal.*, 2017, **7**, 4846–4853.
53 M. F. Baruch, J. E. Pander, J. L. White and A. B. Bocarsly, *ACS Catal.*, 2015, **5**, 3148–3156.
54 A. Dutta, A. Kuzume, M. Rahaman, S. Vesztergom and P. Broekmann, *ACS Catal.*, 2015, **5**, 7498–7502.
55 J. Wu, P. P. Sharma, B. H. Harris and X.-D. Zhou, *J. Power Sources*, 2014, **258**, 189–194.
56 Y. Wang, J. Zhou, W. Lv, H. Fang and W. Wang, *Appl. Surf. Sci.*, 2016, **362**, 394–398.